Fractional Charlier moments for image reconstruction and image watermarking

M. Yamni [a],[*], A. Daoui [b], O. El ogri [a], H. Karmouni [a], M. Sayyouri [b], H. Qjidaa [a], J. Flusser [c]

[a] CED-ST, STIC, Laboratory of Electronic Signals and Systems of Information LESSI, Dhar El Mahrez Faculty of Science, Sidi Mohamed Ben Abdellah-Fez University, Fez, Morocco
[b] Engineering, Systems and Applications Laboratory, National School of Applied Sciences, Sidi Mohamed Ben Abdellah University, BP 72, My Abdallah Avenue Km. 5 Imouzzer Road, Fez, Morocco
[c] Czech Academy of Sciences, Institute of Information Theory and Automation, Pod Vodarenskou vezı 4, 182 08 Praha 8. Czech Republic

ARTICLE INFO

ABSTRACT

In this paper, we propose a new set of discrete orthogonal polynomials called fractional Charlier polynomials (FrCPs). This new set will be used as a basic function to define the fractional discrete orthogonal Charlier moments (FrCMs). The proposed FrCPs are derived algebraically using the spectral decomposition of Charlier polynomials (CPs), then the Lagrange interpolation formula is used to derive the spectral projectors. Then, each spectral projector matrix is decomposed by the singular value decomposition (SVD) technique in order to build a basic set of orthonormal eigenvectors which help to develop FrCPs. FrCMs are deduced in matrix form from the proposed FrCPs and are applied for image reconstruction and watermarking. The experimental results show the capacity of the FrCMs proposed for image reconstruction and image watermarking against different attacks such as noise and geometric distortions.

1. Introduction

Moments have been widely used in image processing and analysis for many years because of their ability to extract characteristic information from the image locally and globally. They are applied with excellent results in different fields such as image reconstruction [1–3,59,60], image compression [3–5], image watermarking [6–10], edge detection [11], image geometric distortion correction [12] and image classification [13,61].

The basic idea of moments is the projection of the data space on often orthogonal bases. Indeed, continuous orthogonal polynomials [14] such as Legendre [15], Zernike [16], Gegenbauer [17] and Fourier–Mellin [18] form continuous orthogonal moments (COMs), and discrete orthogonal polynomials [14,19] such as Tchebichef [20], Krawtchouk [21,22,59,62], Charlier [23–25,59,65], Hahn [23,26,63,66] and Meixner [27,64] constitute discrete orthogonal moments (DOMs).

Generally, the COMs and DOMs of an image are calculated for integer orders but sometimes they have to be calculated for real or fractional orders for reasons of precision and localization of the regions in the image. In this context, work has been performed with the objective of generalizing the calculation of Fourier transform (FT), discrete cosine transform (DCT), discrete sine transform (DST) for real or fractional orders by proposing new transformations such as the Fourier fractional transform (FrFT) [28,29], discrete fractional cosine transform (DFrCT) [30] and the discrete fractional sine transform (DFrST) [30]. The same idea has been developed in recent years for some continuous orthogonal moments. *B. Xiao* et al. [31] developed the fractional Legendre polynomials. *H. Zhang* et al. [32] developed the fractional orthogonal Fourier–Mellin polynomials. *K. Parand* et al. [33] developed the fractional Chebyshev polynomials. The classical case of these polynomials is obtained if the fractional order is equal to the unit. These examples of fractional continuous orthogonal polynomials are used as basic functions to form new fractional continuous orthogonal moments of Legendre [31], Fourier–Mellin [32] and Chebyshev [34].

Fractional continuous orthogonal moments are defined in a Cartesian or polar continuous space, so their calculation requires a discretization of the continuous space and an appropriate approximation of the continuous integrals, which increases the

complexity of the calculations and causes discretization errors [20,22,24,26,27,31,32,34,35] . To avoid these problems, *X. Liu* et al. [7] derived a new fractional Krawtchouk moments (also known as Fractional Krawtchouk Transform FrKT), where the kernel function is fractional Krawtchouk polynomials. To our attention, no other work concerning the other fractional discrete orthogonal moments has been published. With this in mind, we propose in this paper to calculate the fractional orthogonal moments of Charlier in order to apply them for reconstruction and watermarking image tasks.

The discrete orthogonal Charlier moments are calculated from the discrete orthogonal Charlier polynomials. *H. Zhu* et al. [24] proposed two general forms for calculating discrete orthogonal Charlier moments in order to apply them for reconstruction and compression image. *M. Sayyouri* et al. [36] proposed a set of separable Charlier–Hahn invariant moments based on the product of Charlier and Hahn discrete orthogonal polynomials, which are successfully used in pattern recognition and classification of 2D image, due to their robustness against geometric attacks such translation, scaling and rotation. The authors [37,38] and [39] have extended these moments in the 3-D case and have applied them for 3D image reconstruction and classification.

In this paper, we have proposed a new set of discrete orthogonal polynomials called fractional Charlier polynomials (FrCPs), which are used as a basic function to define a new set of fractional Charlier moments (FrCMs). The FrCPs are reduced to the classical Charlier polynomials (CPs) when their fractional order is equal to the unit.

The proposed FrCPs are derived algebraically using first the spectral decomposition of the CPs, then the Lagrange interpolation formula is used to derive the projection matrices of CPs. Next, each projection matrix is decomposed by the singular value decomposition (SVD) technique in order to build a basic set of orthonormal eigenvectors help to develop FrCPs. The FrCPs are used to form new FrCs with additional parameters called fractional orders. Once the mathematical context of the new FrCMs has been developed, image reconstruction and watermarking image are chosen as test applications to verify the practical validity of these new moments. Image reconstruction by FrCMs is achieved through the orthogonality property of FrCPs. The proposed watermarking system consists of two essential phases: insertion and extraction of watermark. In the watermark insertion the fractional orders of the proposed FrCMs are used as security keys. The latter are necessary for the watermark extraction. In order to avoid the errors produced from the truncation of the Charlier polynomial matrix, during the calculation of FrCMs, the Gram-Schmidt process (GSP) is adopted to guarantee the orthogonality property of CPs for any order, which improves the image reconstruction capability by FrCMs. To improve the robustness of the proposed watermarking system to geometric attacks such as rotation and scaling, a technique was adopted to estimate rotational angles and scaling factors. Both FrCMs applications are tested on different images and compared with other recent methods.

The rest of the paper is structured as follows. In Section 2, we recall the definition of the classical discrete orthogonal Charlier moments. Then, we present the new fractional Charlier polynomials and their properties in Section 3. Next, we present the new 1-D and 2-D Fractional Charlier moments in Section 4. As for the Section 5, we introduce a watermarking scheme for 2D images based on the new FrCMs. The experimental results for evaluating the performance of the new FrCMs are given in Section 6, and Section 7 concludes the work.

2. Charlier moments

The discrete orthogonal moments of Charlier are projections of a function f (signal or image) onto the basis of Charlier polynomi-

als (similarly, Fourier transformation is a projection onto a basis of the harmonic functions). In this section, we will present the mathematical background behind the Charlier moment theory, including polynomials, moments and image reconstruction.

2.1. Charlier polynomials

The nth Charlier polynomials (CPs) is defined by using hypergeometric function as [14]:

$$C_n^{a_1}(x) = {}_2F_0(-n, -x; -a_1^{-1}), \quad x, n = 0, 1, 2.....\infty \tag{1}$$

where a_1 is restricted to $a_1 > 0$, and ${}_2F_0()$ is the generalized hypergeometric function given by:

$$_2F_0(a, b; ; c) = \sum_{k=0}^{n} \frac{(a)_k (b)_k (c)^k}{k!} \tag{2}$$

$(a)_k$ is the Pochhammer symbol given by:

$$(a)_k = \begin{cases} 1 & \text{if } k = 0 \\ a(a+1)...(a+k-1) & \text{if } k > 0 \end{cases} \tag{3}$$

The discrete orthogonal polynomials of Charlier $C_n^{a_1}(x)$ satisfy the orthogonality condition:

$$\sum_{x=0}^{\infty} \omega(x) C_n^{a_1}(x) C_m^{a_1}(x) = \rho(n)\delta_{nm}; \; n, m \geq 0 \tag{4}$$

where $\rho(n)$ and $\omega(x)$ are the square norm and the weight function of the CPs, respectively, defined by the following formulas:

$$\rho(n) = \frac{n!}{a_1^n} \tag{5}$$

$$\omega(x) = \frac{e^{-a_1} a_1^x}{x!} \tag{6}$$

To avoid numerical instability when calculating the values of the CPs, the set of weighted CPs noted $\tilde{C}_n^{a_1}(x)$ is used as follows [14]:

$$\tilde{C}_n^{a_1}(x) = C_n^{a_1}(x) \sqrt{\frac{\omega(x)}{\rho(n)}} \tag{7}$$

such that the orthogonality condition becomes [40]:

$$\sum_{x=0}^{\infty} \tilde{C}_n^{a_1}(x) \tilde{C}_m^{a_1}(x) = \delta_{nm}; n, m \geq 0 \tag{8}$$

Like other discrete orthogonal polynomials that can be computed using recursive formulas, the CPs can also be calculated using the following recurrence formula [41]:

$$\tilde{C}_n^{a_1}(x) = -\sqrt{\frac{a_1}{n}} \frac{(x - n + 1 - a_1)}{a_1} \tilde{C}_{n-1}^{a_1}(x)$$

$$\qquad\qquad - \sqrt{\frac{a_1^2}{n(n-1)}} \frac{(n-1)}{a_1} \tilde{C}_{n-2}^{a_1}(x) \tag{9}$$

with

$$\tilde{C}_0^{a_1}(x) = \sqrt{\frac{\omega(x)}{\rho(0)}} \text{ and } \tilde{C}_1^{a_1}(x) = \frac{a_1 - x}{a_1} \sqrt{\frac{\omega(x)}{\rho(1)}} \tag{10}$$

2.2. Charlier moments

Charlier moments (CMs) adopt the name of the CPs which are used during its calculation process. The one-dimensional CMs are defined as [24]:

$$CM_n = \sum_{x=0}^{N-1} \tilde{C}_n^{a_1}(x) f(x) \quad n = 0, 1, ...N - 1 \tag{11}$$

where $f(x)$ is a signal with length N.

If the set of CM_n is given from order 0 up to N, the moment-based signal reconstruction is expressed as follows:

$$f(x) = \sum_{n=0}^{N-1} CM_n \tilde{C}_n^{a_1}(x) \tag{12}$$

The 1-D CMs defined in Eq. (11) can be written in the following matrix form:

$$M = Cf \tag{13}$$

where $M = \{CM_n\}_{n=0}^{n=N-1}$, $C = \{\tilde{C}_n^{a_1}(x)\}_{i=0,x=0}^{n=N-1,x=N-1}$ and $f = \{f(i,j)\}_{i,j=0}^{i,j=N-1}$.

Similarly, the inverse reconstruction procedure can be represented using the matrix form as follows:

$$f = C^T M \tag{14}$$

The 2-D CMs of an $N \times N$ image with intensity function $f(x, y)$ are defined as [1]:

$$CM_{nm} = \sum_{x=0}^{N-1} \sum_{y=0}^{N-1} \tilde{C}_n^{a_1}(x) \tilde{C}_m^{a_1}(y) f(x,y) \quad n, m = 0, 1, \dots N-1 \tag{15}$$

The following matrix notation can be simply used:

$$M = C^T f C \tag{16}$$

where $M = \{CM_{nm}\}_{n=0,m=0}^{n=N-1,m=N-1}$, $C = \{\tilde{C}_n^{a_1}(x)\}_{i=0,x=0}^{n=N-1,x=N-1}$ and $f = \{f(i,j)\}_{i,j=0}^{i,j=N-1}$.

Using the inverse transformation of 2-D CMs, the image function can be reconstructed by the following formula:

$$f(x,y) = \sum_{n=0}^{N-1} \sum_{m=0}^{N-1} \tilde{C}_n^{a_1}(x) \tilde{C}_m^{a_1}(y) CM_{nm} \tag{17}$$

Similarly, the inverse moment transform can be represented using the matrix as follows:

$$f = CMC^T \tag{18}$$

The CPs and CMs introduced into the literature are calculated for integer orders. In the following sections, we propose the calculation of the CPs and CMs for fractional or real orders in order to generalize their calculation and to benefit other properties for non-integer orders.

3. Proposed Fractional Charlier polynomials

In this section, we study the eigenvalues and eigenvectors of CPs which help to develop the new Fractional Charlier Polynomials (FrCPs).

The Charlier polynomials are orthogonal over the interval $[0, \infty[$ according to Eq. (8). To compute the eigenvalues and eigenvectors of the Charlier polynomial matrix, one must work on a square matrix of finite order N which will affect the property of orthogonality of the Charlier polynomials. To solve this truncation problem, we propose to use the Gram–Schmidt process (GSP) [42] which allows to slightly modify the Charlier polynomials in order to make them orthogonal. In the continuation of this work, we will use the GSP-modified Charlier polynomials which are orthogonal over the $[0, N]$ interval, instead of the classical Charlier polynomials.

Algorithm 1 presents the steps of calculating the Charlier polynomial matrix modified by the Gram-Schmidt process (GSP).

3.1. Eigenvalues of the modified Charlier Polynomials

The modified Charlier polynomial matrix will be noted will be noted $\hat{C} = \{\tilde{C}_n^{a_1}(x)\}_{n,x=0}^{n,x=N-1}$ of the order N in the following. The matrix $\hat{C}$ checks the following properties:

Algorithm 1 Orthonormalization of the Charlier polynomial matrix with Gram-Schmidt process.

	Inputs: Parameters Charlier polynomial Output: Modified Charlier polynomial matrix $\hat{C}$

Step 1	for $n = 0 : N - 1$
	   for $x = 0 : N - 1$
	   Using Eq. (10) to compute $\tilde{C}_0^{a_1}(x)$ and $\tilde{C}_1^{a_1}(x)$.
	   end
	end

Step 2	for $n = 2 : N - 1$
	   for $x = 0 : N - 1$
	   Using Eq. (9) to compute $\tilde{C}_n^{a_1}(x)$.
	   $C(x, N) = \tilde{C}_n^{a_1}(x)$

Step 3	for $k = 0 : n$
	   $\tilde{C}_n^{a_1}(x) = \tilde{C}_n^{a_1}(x) - \left[\sum_{x=0}^{N-1} C(x; N)^T \tilde{C}_n^{a_1}(x)\right] \times \tilde{C}_n^{a_1}(x)$
	   end
	   $\widetilde{C}_n^{a_1}(x) = \frac{\tilde{C}_n^{a_1}(x)}{\|\tilde{C}_n^{a_1}(x)\|}$
	   end
	end
	$\hat{C} = \tilde{C}_n^{a_1}(x)$

(a) It is orthogonal, so, $\hat{C}^T \hat{C} = \hat{C}\hat{C}^T = I$, where $\hat{C}^T$ is the transposed matrix of $\hat{C}$ and I is the identity matrix.
(b) It is symmetrical, so $\hat{C} = \hat{C}^T$.
(c) It has the following two eigenvalues:

$$\lambda_1 = +1 \text{ and } \lambda_2 = -1 \tag{19}$$

The proof of *property (c)* is given in Appendix A.

The multiplicities of eigenvalues of the matrix $\hat{C}$ are deduced experimentally as follows: where N is the size of modified Charlier polynomial matrix.

Table 2 presents examples of matrices of Charlier polynomials of order N $\times$ N (N = 2,3, and 4) and their eigenvalues with and without the use of GSP. Fig. 1 shows the sum of the eigenvalues as a function of the size of the matrix of Charlier polynomials modified by GSP and of the matrix of Charlier polynomials ranging from 2 to 30 with a step of 1. These empirical results clearly show that with the use of the Gram–Schmidt process the multiplicities of the eigenvalues $\lambda_1 = 1$ and $\lambda_2 = -1$ are equal (i.e. Trace($\hat{C}$) = 0) for N is even, and for N odd the multiplicity of the eigenvalue $\lambda_1 = 1$ is one more than that of eigenvalue $\lambda_2 = -1$ (i.e. Trace($\hat{C}$) = 1). Furthermore, the eigenvalues of the Charlier polynomial matrix without the use of the Gram–Schmidt process are not 1 and -1 due to truncation errors. Consequently, the Gram–Schmidt process brings the property of orthogonality to order N, destroyed by the truncation of Charlier polynomials to order N.

3.2. Spectral decomposition of modified Charlier polynomials

According to the spectral theorem [43], $\hat{C}$ has the following spectral decomposition:

$$\hat{C} = \sum_{k=1}^{2} \lambda_k P_k = \lambda_1 P_1 + \lambda_2 P_2 \tag{20}$$

where P_k denotes the spectral projector for $\hat{C}$ associated with the eigenvalue λ_k. Also, for any integer m, $\hat{C}^m$ has the following spectral decomposition [43]:

$$\hat{C}^m = \lambda_1^m P_1 + \lambda_2^m P_2 \tag{21}$$

In the following, we will present a method to derive the two projection matrices P_1 and P_2.

According to the corollaries of the spectral theorem [44, p. 403], each spectral projector matrix P_k can be expressed as:

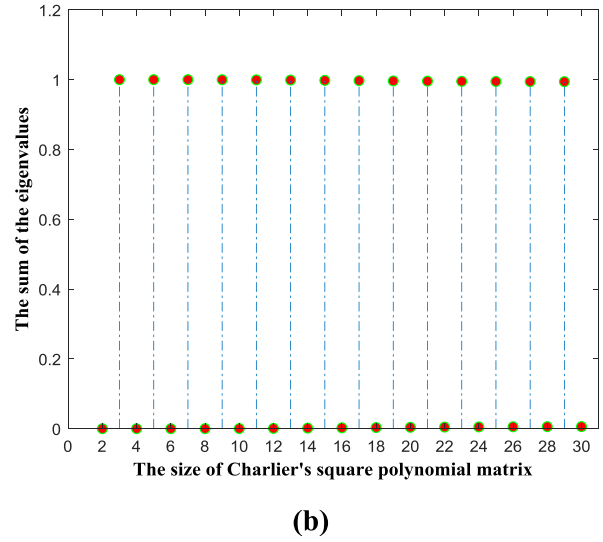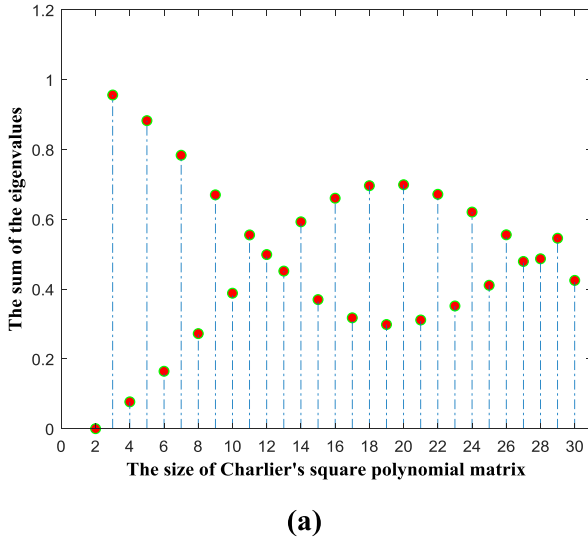$$P_k = g_k(\hat{C}) \quad k = 1, 2 \tag{22}$$

Fig. 1. Sum of eigenvalues as a function of matrix size of Charlier polynomials (a) classical and (b) modified by GSP.

where $g_k(\hat{C})$ is a polynomial in $\hat{C}$, which satisfies the following condition:

$$g_k(\lambda_i) = \delta_{i,k} \quad i = 1, 2 \tag{23}$$

Since matrix $\hat{C}$ has only two eigenvalues, the polynomial $g_k(\hat{C})$ is of the first degree. Using the Lagrange interpolation formula, $g_k(\lambda)$ can be expressed as:

$$g_k(\lambda) = \sum_{i=1}^{2} g_k(\lambda_i) f_i(\lambda)$$
$$= g_k(\lambda_1) f_1(\lambda) + g_k(\lambda_2) f_2(\lambda) \tag{24}$$

where

$$f_i(\lambda) = \prod_{\substack{r=1 \\ r \neq i}}^{2} \frac{\lambda - \lambda_r}{\lambda_i - \lambda_r} \quad i = 1, 2 \tag{25}$$

By combining Eqs. (23), (24) and (25), we obtain:

$$g_k(\lambda) = f_k(\lambda) = \prod_{\substack{r=1 \\ r \neq k}}^{2} \frac{\lambda - \lambda_r}{\lambda_k - \lambda_r} \tag{26}$$

By substituting Eq. (19) in the above equation, we find:

$$g_1(\lambda) = \frac{\lambda - \lambda_2}{\lambda_1 - \lambda_2} = 0.5(1 + \lambda) \tag{27}$$

$$g_2(\lambda) = \frac{\lambda - \lambda_1}{\lambda_2 - \lambda_1} = 0.5(1 - \lambda) \tag{28}$$

Using Eqs (22),(27) and (28), we get the following expressions for the projection matrices P_1 and P_2:

$$P_1 = 0.5(I + \hat{C}) \tag{29}$$

$$P_2 = 0.5(I - \hat{C}) \tag{30}$$

In the following, we will study the eigenvalues and the eigenvectors of the two spectral projector matrices P_1 and P_2, then we will present their properties.

From Eqs. (29) and (30), P_1 and P_2 satisfy the following properties:

(d) $P_i^T = P_i, i = 1, 2$

(e) $P_i^2 = P_i, i = 1, 2$.
(f) $P_1 P_2 = 0$, where 0 denotes the zero matrix.

The proof of *properties (d)–(f)* is given in Appendix B.

(g) The eigenvalues of a projection matrix P_1 and P_2 are only 0 and 1 [45].
(h) The #(1) of P_1 is equal to #(λ_1) of the matrix $\hat{C}$; and the #(1) of P_2 is equal to #(λ_2) of the matrix $\hat{C}$, where #(.) indicates the multiplicity of an eigenvalue.

The proof of *property (h)* is given in Appendix B.

Lemma 1. *For the non-zero eigenvalues: The eigenvectors of P_1 are orthogonal to those of P_2.*

Lemma 2. *For the non-zero eigenvalues: the eigenvectors of P_1 and P_2 are the eigenvectors of $\hat{C}$, corresponding to eigenvalues $\lambda_1 = 1$, $\lambda_2 = -1$ of $\hat{C}$, respectively.*

The proofs of both *Lemmas 1* and *2* are given in Appendix $\hat{C}$.

In the following, we will derive a set of orthonormal eigenvectors of $\hat{C}$ by using the singular-value decomposition (SVD) of its orthogonal projection matrices on its eigenspaces [45].

The SVD of P_1 and P_2 are given as:

$$P_1 = U_1 S_1 V_1^T \tag{31}$$

$$P_2 = U_2 S_2 V_2^T \tag{32}$$

where U_i and $V_i (i = 1, 2)$ are unitary matrices and S_i a diagonal matrix with real and positive coefficient.

Using properties (a), (b) and (g), we can easily rewrite the Eqs. (31) and (32) as follows:

$$P_1 = V_1 S_1 V_1^T \tag{33}$$

$$P_2 = V_2 S_2 V_2^T \tag{34}$$

It can be observed from (33) and (34) that:

$$P_1 V_1 = S_1 V_1; \; P_2 V_2 = S_2 V_2 \tag{35}$$

The above equation shows that V_1 and V_2 are a set of orthonormal eigenvectors of P_1 and P_2, respectively.

According to Table 1 and proprieties (g) and (h), the multiplicities of the non-zero eigenvalues for P_1 and P_2 are summarized for an $N \times N$ transform in Table 3.

Table 1
Multiplicities of the eigenvalues for matrix $\hat{C}$.

N	Multiplicity of λ_1	Multiplicity of λ_2
Even	$\frac{N}{2}$	$\frac{N}{2}$
Odd	$\frac{N+1}{2}$	$\frac{N-1}{2}$

Table 3
Multiplicities of the non-zero eigenvalues for P_1 and P_2.

P_k	N	
	Even	Odd
P_1	$\frac{N}{2}$	$\frac{N+1}{2}$
P_2	$\frac{N}{2}$	$\frac{N-1}{2}$

According to the Table 3 and *Lemma 2*, we are now ready to derive a set of orthonormal eigenvectors of $\hat{C}$.

Taking u_i and v_j be the ith and jth column of V_1 and V_2, respectively, a set of orthonormal eigenvectors V of $\hat{C}$ can be written as follows:

$$V = \begin{cases} \left[u_1, u_2, ..., u_{\frac{N}{2}}, v_1, v_2, ..., v_{\frac{N}{2}}\right], & \text{if } N \text{ is even} \\ \left[u_1, u_2, ..., u_{\frac{N-1}{2}}, u_{\frac{N+1}{2}}, v_1, v_2, ..., v_{\frac{N-1}{2}}\right], & \text{if } N \text{ is odd} \end{cases} \tag{36}$$

3.3. Proposed fractional Charlier polynomials

Based on these results, we are now ready to propose a new set of Fractional Charlier polynomials (FrCPs).

Firstly, the columns of V can be rearranged to match eigenvectors to eigenvalues of $\hat{C}$ as follows:

$$\hat{V} = \begin{cases} \left[u_1, v_1, u_2, v_2 .... u_{\frac{N}{2}}, v_{\frac{N}{2}}\right], & \text{if } N \text{ is even} \\ \left[u_1, v_1, u_2, v_2 .... u_{\frac{N-1}{2}}, v_{\frac{N-1}{2}}, u_{\frac{N+1}{2}}\right], & \text{if } N \text{ is odd} \end{cases} \tag{37}$$

Then, Charlier polynomial matrix $\hat{C}$ can be written as follows:

$$\hat{C} = \hat{V}D\hat{V}^T \tag{38}$$

where D is the diagonal matrix whose diagonal elements are the eigenvalues of $\hat{C}$. From the *propriety (c)* and Table 1 we have:

$$D = \begin{cases} Diag\{1, -1, 1, -1........1, -1\}, & \text{if } N \text{ is even} \\ Diag\{1, -1, 1, -1........1, -1, 1\}, & \text{if } N \text{ is odd} \end{cases} \tag{39}$$

Also, the matrix D can be written as $e^{-jk\pi}$ with $k = 0, 1, ..., N-1$ as follows:

$$D = Diag\{1, e^{-j\pi}, e^{-j2\pi}, ..., e^{-j(N-2)\pi}, e^{-j(N-1)\pi}\} \tag{40}$$

Adopting the same idea as that in [46], the Fractional Charlier polynomials (FrCPs) as the generalized version of the Charlier polynomials can be produced by taking the fractional order as the power of the diagonal matrix D.

Finally, the FrCP matrix $\hat{C}^a$ of size N with order a can be defined as:

$$\hat{C}^a = \hat{V}D^a\hat{V}^T = \sum_{k=0}^{N-1} e^{-jka\pi}\hat{v}_k\hat{v}_k^T \tag{41}$$

where $\hat{V} = [\hat{v}_0, \hat{v}_1, ..., \hat{v}_{N-1}]$ with $\hat{v}_k(k = 0, 1, ..., N-1)$ is the $\hat{C}$ eigenvector obtained from Eq. (37), and D^a is defined as:

$$D^a = Diag\{1, e^{-ja\pi}, e^{-j2a\pi}, ..., e^{-j(N-1)a\pi}\} \tag{42}$$

The properties of FrCP matrix are discussed in the following subsection.

3.4. Some properties of fractional Charlier polynomials matrix

FrCP fractional Charlier polynomials have four important properties which allow us to find classic Charlier polynomials from FrCP for case $a = 1$, calculate FrCPs of order $a + b$ from a simple multiplication of FrCP of order a and of FrCP of order b, calculate the inverse FrCP of order a from the FrCP of order $-a$. These properties of the matrix FrCP can be easily verified as follows:

- $\hat{C}^0 = \hat{V}D^0\hat{V}^T = \hat{V}\hat{V}^T = I$, where I is the identity matrix.
- $\hat{C}^1 = \hat{V}D^1\hat{V}^T = \hat{V}D\hat{V}^T = \hat{C}$, where $\hat{C}$ is the classical Charlier polynomial matrix.
- $\hat{C}^a\hat{C}^b = (\hat{V}D^a\hat{V}^T)(\hat{V}D^b\hat{V}^T) = \hat{V}D^{a+b}\hat{V}^T = \hat{C}^{a+b}$.
- $\hat{C}^{-a} = (\hat{C}^a)^{-1}$, because $\hat{C}^a\hat{C}^{-a} = (\hat{V}D^a\hat{V}^T)(\hat{V}D^{-a}\hat{V}^T) = \hat{V}D^{a-a}\hat{V}^T = I$.

The FrCPs depend on two parameters a_1 and a which can offer a wide choice in applications where FrCPs are used, compared to classical CPs which depend on a single parameter a_1. When the fractional order a of FrCPs is unity, we get the CPs.

4. Proposed Fractional Charlier moments

The generalized Fractional Charlier Moments (FrCMs) are obtained from the FrCPs developed in the previous section.

Based on Eq. (13), the 1-D FrCMs of signal $f(x)$ with fractional order a can be defined as follows:

$$M^a = \hat{C}^a f \tag{43}$$

Table 2
Eigenvalues of Charlier polynomial matrices: classical and modified by GSP.

| Size	Classical Charlier Polynomials matrix	Modified Charlier Polynomials matrix
$N = 2$	$C = \begin{pmatrix} 0,99005 & 0,140014 \\ 0,140014 & -0,97025 \end{pmatrix}$ eig(C) = [−0,9802; 1]; Trace(C) = 0.0198	$\hat{C} = \begin{pmatrix} 0,990148 & 0,140028 \\ 0,140028 & -0,99015 \end{pmatrix}$ eig($\hat{C}$) = [−1; 1]; Trace($\hat{C}$) = 0
$N = 3$	$C = \begin{pmatrix} 0,985112 & 0,170626 & 0,020897 \\ 0,170626 & -0,95556 & -0,23768 \\ 0,020897 & -0,23768 & 0,926449 \end{pmatrix}$ eig(C) = [−1; 1; 0,956]; Trace(C) = 0,956002	$\hat{C} = \begin{pmatrix} 0,985114 & 0,170663 & 0,0206 \\ 0,170627 & -0,95619 & -0,23786 \\ 0,020897 & -0,23784 & 0,97108 \end{pmatrix}$ eig($\hat{C}$) = [−1; 1; 1]; Trace($\hat{C}$) = 1
$N = 4$	$C = \begin{pmatrix} 0,980199 & 0,19604 & 0,027724 & 0,003201 \\ 0,19604 & -0,94099 & -0,2717 & -0,04738 \\ 0,027724 & -0,2717 & 0,902567 & 0,326059 \\ 0,003201 & -0,04738 & 0,326059 & -0,86492 \end{pmatrix}$ eig(C) = [−1; −0,92313; 1; 0,999987]; Trace(C) = 0,076858	$\hat{C} = \begin{pmatrix} 0,980199 & 0,196042 & 0,027724 & 0,003083 \\ 0,19604 & -0,94101 & -0,2719 & -0,04624 \\ 0,027724 & -0,2717 & 0,904708 & 0,326975 \\ 0,003201 & -0,04738 & 0,326811 & -0,9439 \end{pmatrix}$ eig($\hat{C}$) = [−1; −1; 1; 1]; Trace($\hat{C}$) = 0
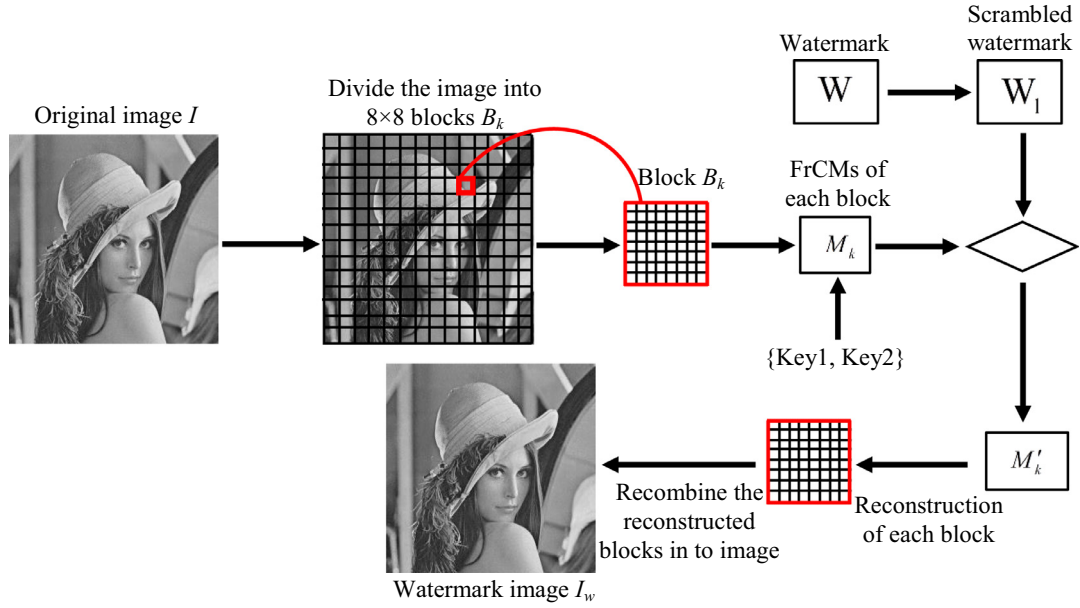
Fig. 2. The watermark embedding scheme based on FrCMs.
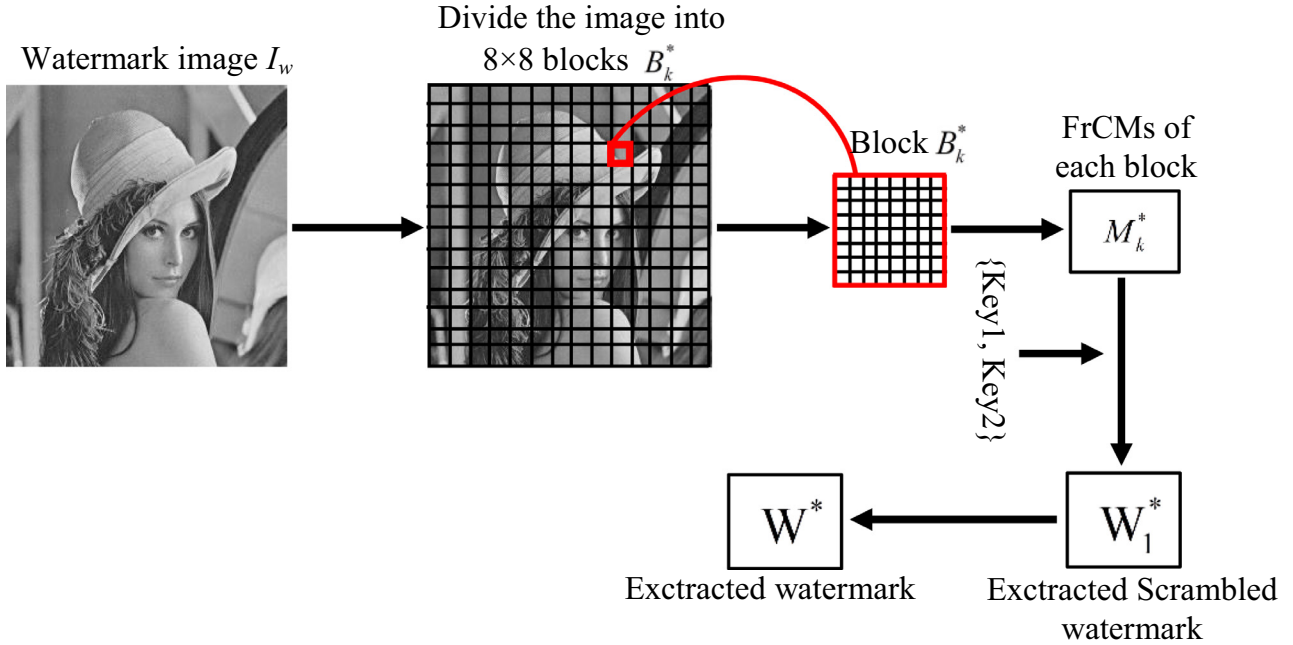

Fig. 3. The watermark extraction scheme based on FrCMs.

Based on Eq. (14) and *property (a)*, the reconstruction of the signal $f(x)$ can be found from its moments by using the following expression:

$$f = \hat{C}^{-a}M^a \qquad (44)$$

In 2-D case, the FrCMs in terms of FrCPs with fractional order (a, b), for an image with intensity function $f(x, y)$, can be defined as follows:

$$M^{a,b} = \hat{C}^a f \hat{C}^b \qquad (45)$$

The Eq. (45) leads to the following inverse reconstruction procedure:

$$f = \hat{C}^{-a}M^{a,b}\hat{C}^{-b} \qquad (46)$$

5. Images watermarking system using fractional Charlier moments

Digital watermarking is a vast field that combines a large range of applications such as authentication, copyright protection, fingerprint, copy control and broadcast monitoring [47].

The basic idea of digital watermarking is to incorporate some information's (called watermark or message) into another data file (Audio, image, video, 3D objects, etc.) called the host. Incorporation is done by imperceptible modifications on the host, so that the watermarked host can replace the original for practical purposes.

In this paper, we apply the proposed FrCMs in the copyright protection application for 2D digital images. For this type of application, the digital watermark should have properties such as im-
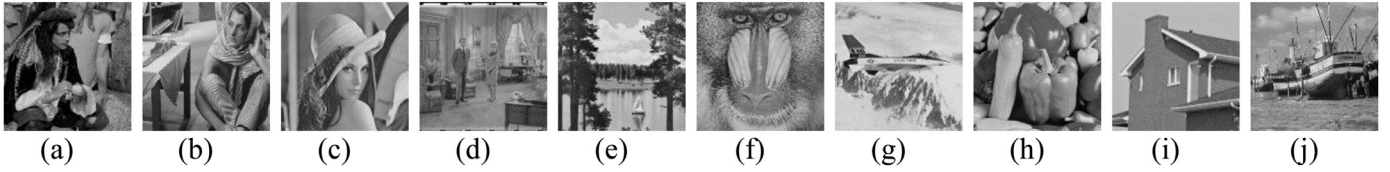
Fig. 4. Test grayscale images used in experiments; (a) Male, (b) Barbara, (c) Lena, (d) Couple, (e) Sailboat on lake, (f) Mandrill, (g) Airplane, (h) Peppers, (i) House and (j) Boat.
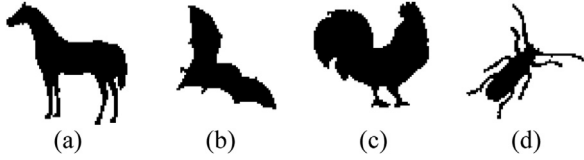

Fig. 5. Digital watermarks extracted from [58] used in watermark experimentations, (a) Horse, (b) Bat, (c) Chicken and (d) Beetle.

perceptibility of detection, high detection reliability, and robustness against signal processing and geometric attacks [47].

Generally, image watermarking systems for copyright protection can be divided into:(i) Systems based on watermark schemes in the spatial domain where the watermark is directly incorporated by modifying the pixel values of the host image. These systems are relatively weak in the event of an image attack (image filtering, compression, etc.) [47]. (ii) Systems based on watermark schemes in the transform domain where the watermark is incorporated after the transformation of the host image into a transformation domain.

In order to increase the robustness of systems against signal processing and geometric attacks, researchers focus on watermarking systems in the transform domain, such that DFT transform [48], DCT transform [49], DST transform, SVD transform [50],quaternion Fourier transform [51], also, recent works based on discrete orthogonal moments transformations have been published such as Tchebichef moments [9,10,52], Krawtchouk moments [6], separable moments [6,9] and fractional moments of Krawtchouk [7].

In this section, we will propose an image watermarking system based on the proposed FrCMs, offering good visual quality and reasonable resistance against signal processing and geometric attacks. This system consists of two essential phases: the insertion

Fig. 6. Average PSNR of the 40 watermarked images with different quantization steps for various watermarking schemes.

Fig. 7. Watermarked "Male" images with the quantization step $\Delta = 30$ using the watermark embedding scheme based on: (a) FrCMs, PSNR =58,78 dB, (b) FrCMs without GSP, PSNR = 49.5473 dB, and (c) based on CMs, PSNR = 42.88 dB.
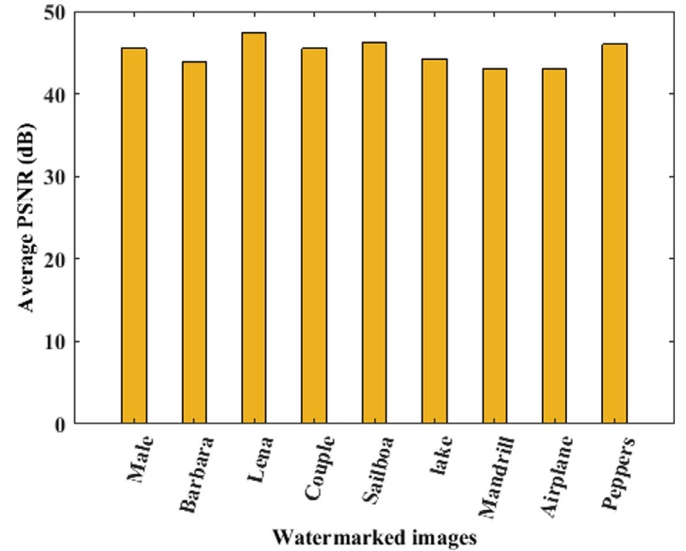

Fig. 8. Average PSNR of the watermarked images with the quantization step $\Delta = 60$ using the watermark embedding scheme based on the proposed FrCMs.

and extraction of watermarks. The description of these phases will be presented in the following subsections.

5.1. Watermark insertion scheme

Let $I = \{f(x, y), (0 \leq x, y < N)\}$ denotes a host gray-scale image, and $f(x, y)$ is the pixel value at position(x, y). $W = \{w(i, j), (0 \leq i, j < l)\}$ denotes a binary image to be embedded within the host image, and $w(i, j) \in \{0, 1\}$ is the pixel value at position (i, j).

The watermark insertion scheme based on FrCMs is shown in Fig. 2, and is described below:

Step 1: Watermark preprocessing

Before watermark insertion, some preprocessing methods can be added for improving the efficiency of watermarking system. In this context, to ensure the security of the watermark and to improve the robustness of our watermarking system, the watermark
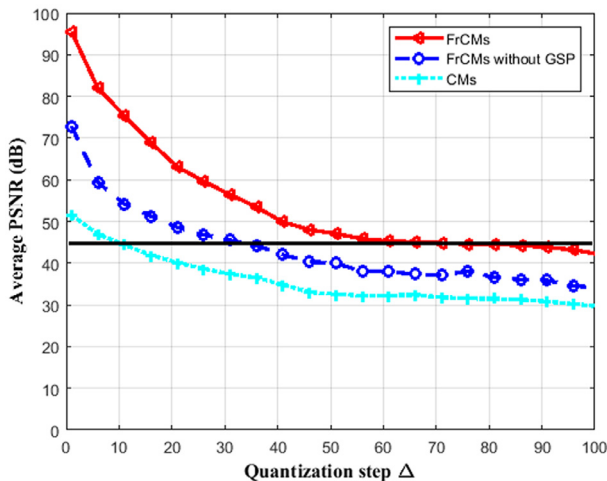
is scrambled from W into W_1 by using the following Arnold transform [53,54]:

$$\begin{bmatrix} x' \\ y' \end{bmatrix} = \begin{bmatrix} 1 & 1 \\ k & k+1 \end{bmatrix} \begin{bmatrix} x \\ y \end{bmatrix} \bmod (N) \tag{47}$$

where (x, y) and (x', y') are the pixels of W and W_1, respectively. N represents the image size and k a control parameter. This parameter can be used as private key during the watermark extraction process.

Step 2: Host image blocking

The host image I is divided into small blocks B_k of size 8×8 pixels:

$$B_k = \{b_k(i,j), 0 \le i, j < 7\} \quad (k = 1, 2, \dots N^2/64) \tag{48}$$

Step 3: Fractional Charier Moments

The FrCMs are computed for each block $B_k(k = 1, 2, \dots N^2/64)$ by using the following equation:

$$M^{a,b} = C^a B_k C^b, k = 1, 2, \dots N^2/64 \tag{49}$$

The FrCMs matrix of one block is denoted M.

The two polynomial parameters a_1 and b_1, and the fractional orders a and b are used to reinforce the security of our watermark scheme. These values are denoted Key1.

Step 4: Watermark embedding

In our scheme, the watermark bit embedding strategy is adopted. Once the matrix FrCMs of each block is calculated, the watermark bits are embedded into the host image blocks by modifying the modulus of the coefficients of the real part M_0 of M using the following quantization function [55,56]:

$$|M_0'(\text{key1, key2})|$$
$$= \begin{cases} 2\Delta \times round\left(\frac{|M_0(\text{key1,key2})|}{2\Delta}\right) + \frac{\Delta}{2}, & \text{if } W_1(i,j) = 1 \\ 2\Delta \times round\left(\frac{|M_0(\text{key1,key2})|}{2\Delta}\right) - \frac{\Delta}{2}, & \text{if } W_1(i,j) = 0 \end{cases} \tag{50}$$

where Key2 denotes the positions of the selected pixels in the blocks that constitute the second secret key, and M_0 is the old real part FrCMs matrix of one block, M_0' is the new FrCMs matrix of this block, and Δ is the quantization step controlling the embedding strength of the watermark bit.

Note that, for a gray-scale image of size 512×512, the total number of bits that can be embedded is 4096. Therefore, the size of the watermark must be equal or small than 64×64 ($64 \times 64 = 4096$ bits).

Step 5: Obtaining the watermarked image.

The inverse operation of FrCMs is applied on each new block M_0' to obtain the watermarked image.

Although, the image watermarking system must have good visual quality and reasonable resistance against signal processing and geometric attacks. Some attacks, such as rotation and scaling, can greatly affect the precision of watermark extraction. This is because, the rotation operation moves the pixels and some of them are permanently damaged according to the rotation angle, and for the scaling operation, the pixel values of an image are replaced or interpolated in a local neighborhood. Therefore, in order to extract the watermark correctly, the rotation angle and scale factor of the attacked image can be estimated to recover the attacked image in its original form. In this paper, the technique presented in [57] is adopted to ensure the robustness against these geometric attacks. For more details, see Ref. [6].
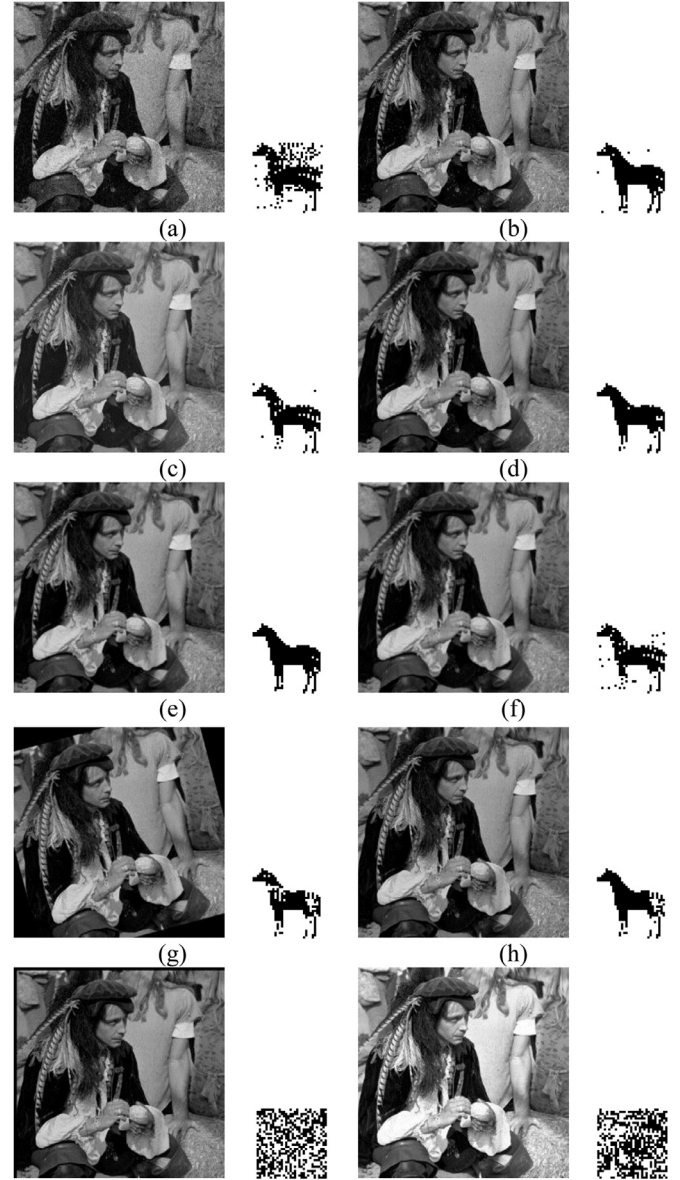

Fig. 9. The attacked watermarked "Male" image and the extracted "Horse" watermark: (a) Gaussian White Noise ($\mu = 0$, $\sigma = 1\%$), BER = 0.1623, (b) Salt & peppers noise (1%), BER = 0.0117, (c) JPEG 60, BER = 0.04785, (d) Median filtering (3×3), BER = 0.02050, (e) Average filtering (3×3), BER = 0.0107, (f) Gaussian blur (1), BER = 0.066, (g) Rotation (15°), BER = 0.06738, (h) Scaling (1.1), BER = 0.04785, (i) Translation (+7,+7), BER = 0.481445, (j) Histogram equalization(150), BER = 0.49609.

5.2. Watermark extraction scheme

The watermark extraction procedure in the proposed system needs the main security information {Key1, Key2} to extract correctly the watermark. Fig. 3 shows the main steps of watermark extraction which can be described in the following:

Step 1: Watermarked image blocking

Let I_w denotes the watermarked image. The I_w is divided into small blocks B_k^* of size 8×8 pixels

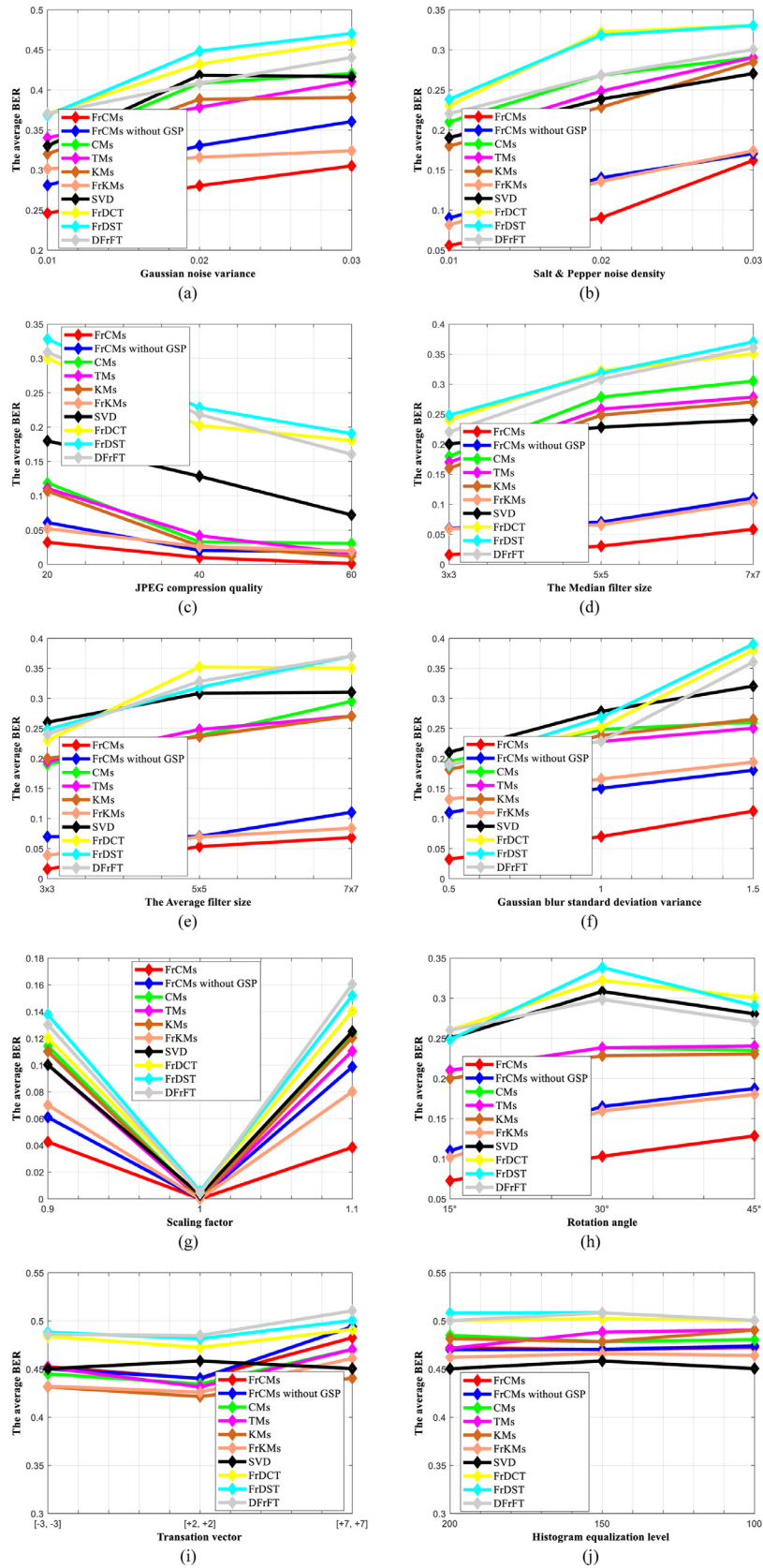$$B_k^* = \{b_k^*(i,j), 0 \le i, j < 7\} \quad (k = 1, 2, \dots N^2/64) \tag{51}$$

Fig. 10. The watermark extraction results of different watermarking schemes for signal processing attacks and geometric ones (BER).

Table 4
The average reconstruction errors based on MSE / PSNR values, of the test images shown in Fig. 4 by using the proposed FrCMs, FrCMs without GSP and classical CMs.

Moments	Average MSE	Average PSNR
FrCMs ($a = b = 0.3$)	2.6323E-24	283.92
FrCMs ($a = b = 0.7$)	4.1694E-24	281.93
FrCMs without GSP ($a = b = 0.3$)	1.1986E-6	107.34
FrCMs without GSP ($a = b = 0.7$)	6.8887E-6	99.74
CMs	6.4310E-3	70.04

Step 2: Fractional Charier moments

The FrCMs matrix M^* is computed for each watermarked block B_k^*:

$$M^* = C^a B_k^* C^b, (k = 1, 2, ...N^2/64) \qquad (52)$$

Step 3: watermark extraction

With the same keys (Key1, Key2) as in the process of watermark insertion, the following function is used to extract one bit of watermark at position(i, j):

$$W_1^*(i, j)$$
$$= \begin{cases} 1 \ if \ |M_0^*(\text{key1, key2})| - 2\Delta \times round\left(\frac{|M_0^*(\text{key1,key2})|}{2\Delta}\right) > 0 \\ 0 \ if \ |M_0^*(\text{key1, key2})| - 2\Delta \times round\left(\frac{|M_0^*(\text{key1,key2})|}{2\Delta}\right) \leq 0 \end{cases}$$
$$(53)$$

where M_0^* is the real part of M^* and W_1^* is the extracted scrambled watermark.

Step 4: Obtaining the extracted watermark.

The extracted watermark can be obtained by descrambling W_1^* to W^* by using the inverse Arnold transform.

6. Simulation results

In this section we will provide an experimental validation of the theoretical framework presented in this paper. This section is divided into two sub-sections. In the first subsection, we will test the ability of the proposed FrCMs for the reconstruction of 2D images. In the second part, we will test the imperceptibility and the robustness of the proposed watermarking scheme against signal processing and geometric attacks. Several functions are used to qualify the proposed FrCMs:

The Peak-Signal-to-Noise Ratio (PSNR) is used to assess the quality of the watermarked image or the reconstructed image, by finding the difference between these images and the original image. PSNR is defined as follows:

$$PSNR = 10\log_{10}\frac{255^2}{MSE} \qquad (54)$$

where MSE is the Mean Square Error given by:

$$MSE = \frac{1}{N \times N} \sum_{i=1}^{N-1}\sum_{j=1}^{N-1}\left(I(i, j) - I'(i, j)\right)^2 \qquad (55)$$

whit $I(x, y)$ is the original image and $I'(x, y)$ is the watermarked image or the reconstructed image.

The Bit Error Rate (BER) is used to measure the similarity between the original watermark W and the extracted one W^*. Lesser the BER, more robust the watermark is towards the attacks. BER is defined as:

$$BER = \frac{1}{l \times l} \sum_{i=1}^{l}\sum_{j=1}^{l} |W^*(i, j) - W(i, j)| \qquad (56)$$

All algorithms in this paper are implemented in MATLAB R2015a, and all numerical experiments are performed under Microsoft Windows environment on a PC with Intel Core i3 CPU 2.4 GHz and 3 GB RAM.

6.1. Image reconstruction

In this subsection, a comparative study between the proposed FrCMs and the classical CMs is performed in terms of image reconstruction without and with the Gram-Schmidt process (GSP). The PSNR and MSE are used as criteria to evaluate the quality of the reconstructed images. To do this, a set of ten gray-scale images (Fig. 4) of size 512 × 512 is used in this test. Table 4 shows the average reconstruction errors, based on the MSE and PSNR values of all test images, using the proposed FrCMs and proposed FrCMs without GSP with fractional orders: ($a = b = 0.3$) and ($a = b = 0.7$), and the classical CMs ($a = b = 1$). Knowing that the reconstruction order is the size of the images for all types of moments used in this test. Table 5 shows some examples of reconstructed images and their MSE / PSNR values using these moments.

It is clear from these results that the image reconstruction errors of the proposed FrCMs are very small compared to the errors obtained by the other types of moments, especially in the case of a good choice of fractional orders of FrCMs. It can be seen that the image reconstruction quality improves considerably with the use of GSP when calculating FrCMs. This shows the effectiveness of this process in correcting digital errors and preserving the orthogonality property when calculating FrCPs, which positively reflects on the quality of the reconstructed images. Moreover, these results further show that FrCMs with some fractional orders can give better reconstruction results than Charlier's classical moments (of integer fractional orders).

This experiment validates the mathematical development presented in this paper and demonstrates the ability of the proposed FrCMs to reconstruct images with excellent results. Once the capacity of moments proposed for image reconstruction has been demonstrated, these descriptors will be applied for applications that use image reconstruction such as image watermarking where image reconstruction is a necessary step in the watermark insertion phase.

6.2. Image watermarking

In this subsection, the watermarking system based on the proposed FrCMs is examined for various signal processing attacks as well as for some geometric attacks. Table 6 presents the attacks our watermark experimentations. The ten gray-scale test images (Fig. 4) are used as host images and the four binary images of size 64 × 64 are shown in Fig. 5 as test watermarks.

In the first test, we will study the imperceptibility of the proposed watermark scheme based on FrCMs. Each of the four test watermarks is incorporated into the ten test images using the watermark embedding scheme (Fig. 2). A total of 40 watermarked images are generated, each watermarked image is compared to the corresponding original image using the PSNR as a criterion, for a quantization step Δ ranging from 1 to 100 with an increment equal to 5. The average PSNR values are represented according to the quantization step in Fig. 6 for the fractional orders ($a = b = 0.3$) of the FrCMs. Our scheme is also compared to the watermark scheme based on FrCMs without GSP and that based on classical CMs. The results are presented in the same figure (Fig. 6) to facilitate comparison. Fig. 7 shows an example of the watermarked "Male" images obtained using these schemes for the quantization step $\Delta = 30$.

Figs. 6 and 7 show that the schemes based on the proposed FrCMs give the best results for all quantization steps in terms of

Table 5
The reconstructed images of "Male" and "Mandrill" and their MSE/PSNR values yielded by using the proposed FrCMs, FrCMs without GSP and classical CMs.

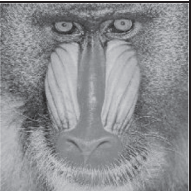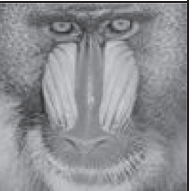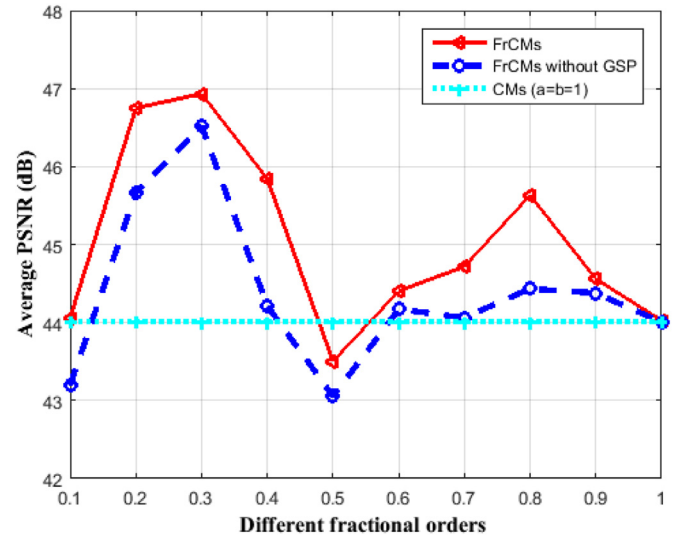| Images	FrCMs ($a = b = 0.3$)	FrCMs ($a = b = 0.7$)	FrCMs without GSP ($a = b = 0.3$)	FrCMs without GSP ($a = b = 0.7$)	CMs
Male	MSE=1.66E-24 PSNR=285.92dB	MSE=1.32E-24 PSNR=285.92dB	MSE=1.76E-05 PSNR=95.66dB	MSE=1.56E-05 PSNR=96.19dB	MSE=2.48E-05 PSNR=64.18dB
Mandrill	MSE=1.58E-24 PSNR=286.13dB	MSE=1.36E-24 PSNR= 286.13dB	MSE=3.46E-05 PSNR=92.72dB	MSE=9,86E-05 PSNR=88.19dB	MSE=3.50E-05 PSNR=62.69Db

Table 6
Information of the applied attacks.

Attacks	Parameters
Gaussian White Noise	Variance: 1%, 2%, 3%
Salt & Peppers Noise	Density: 1%, 2%, 3%
JPEG compression	Quality: 20%, 40%, 60%
Median filtering	Kernel size: 3×3, 5×5, 7×7
Average filtering	Kernel size: 3×3, 5×5, 7×7
Rotation	Rotation angle: 15°, 30°, 45°
Scaling	Scaling factor: 0.9, 1, 1.1
Translation	Translation vector: $(-3,-3)$, $(+2,+2)$, $(+7,+7)$
Gaussian blur	Standard derivation: 0.5, 1, 1.5

Fig. 11. Average PSNR of watermarked images with different fractional orders.

transparency, especially when the GSP is applied. Opposite to the scheme based on classical CMs which gives low quality of watermarked images. It is obvious that watermarked images are very close to the originals for the low quantization steps, and the difference between these images is relatively large when the high quantization steps are used.

In order to make a fair comparison with other methods in the following experiments, the quantization step Δ is chosen to maintain an acceptable PSNR of about 45 dB. We will use $\Delta = 60$, $\Delta = 35$ and $\Delta = 10$ for schemes based on: FrCMs, FrCMs without GSP and classical CMs, respectively. The average quality of the watermarked images (four watermarked images for each host image) using our FrCMs scheme for $\Delta = 60$ is shown in Fig. 8.

In the second test, we will test the robustness of the proposed FrCMs watermark scheme against the signal processing and geometric attacks presented in Table 6. Each of the 40 watermarked images is distorted according to these attacks, then the watermark is extracted using the watermark extraction scheme shown in Fig. 3. The test is performed for the fractional orders ($a = b = 0.3$) and the quantization step $\Delta = 60$. Fig. 9 shows some examples of watermarked "Male" images distorted by the attacks used and the extracted "Horse" watermarks with their corresponding BER values.

The robustness of this scheme is compared to that of the scheme based on FrCMs without GSP and to that of the scheme based on classical CMs. The average BER values obtained from these schemes are shown in Fig. 10. In addition, these schemes are compared with schemes based on: Tchebichef moments (TMs) [9],

Krawtchouk moments (KMs) [6], Krawtchouk fractional moments (FrKMs) [7], SVD transformation [45], discrete fractional Fourier transform (DFrFT), discrete fractional cosine transform (DFrCT) and discrete fractional sine transform (DFrST).

By examining Figs. 10(a–h), it is clear that the scheme based on the proposed FrCMs provides very satisfactory results for most attacks, such as white Gaussian noise, salt & peppers noise, median filtering, average filtering, JPEG compression, rotation and scaling, where the BER values are very low, indicating that the extracted watermarks can be easily recognized after these attacks and are very close to the originals as shown in examples Figs. 9(a–h). However, according to Figs. 10(i and j), this scheme is not very robust against translation and histogram equalization attacks where the difference between the extracted watermarks and originals is relatively important as shown in examples Figs. 9(i and j).

This is due on the one hand to the approach of the blocks used by our scheme which does not allow to extract correctly the watermark in the case of translation because of change of the positions blocks of image. On the other hand, the adopted embedding
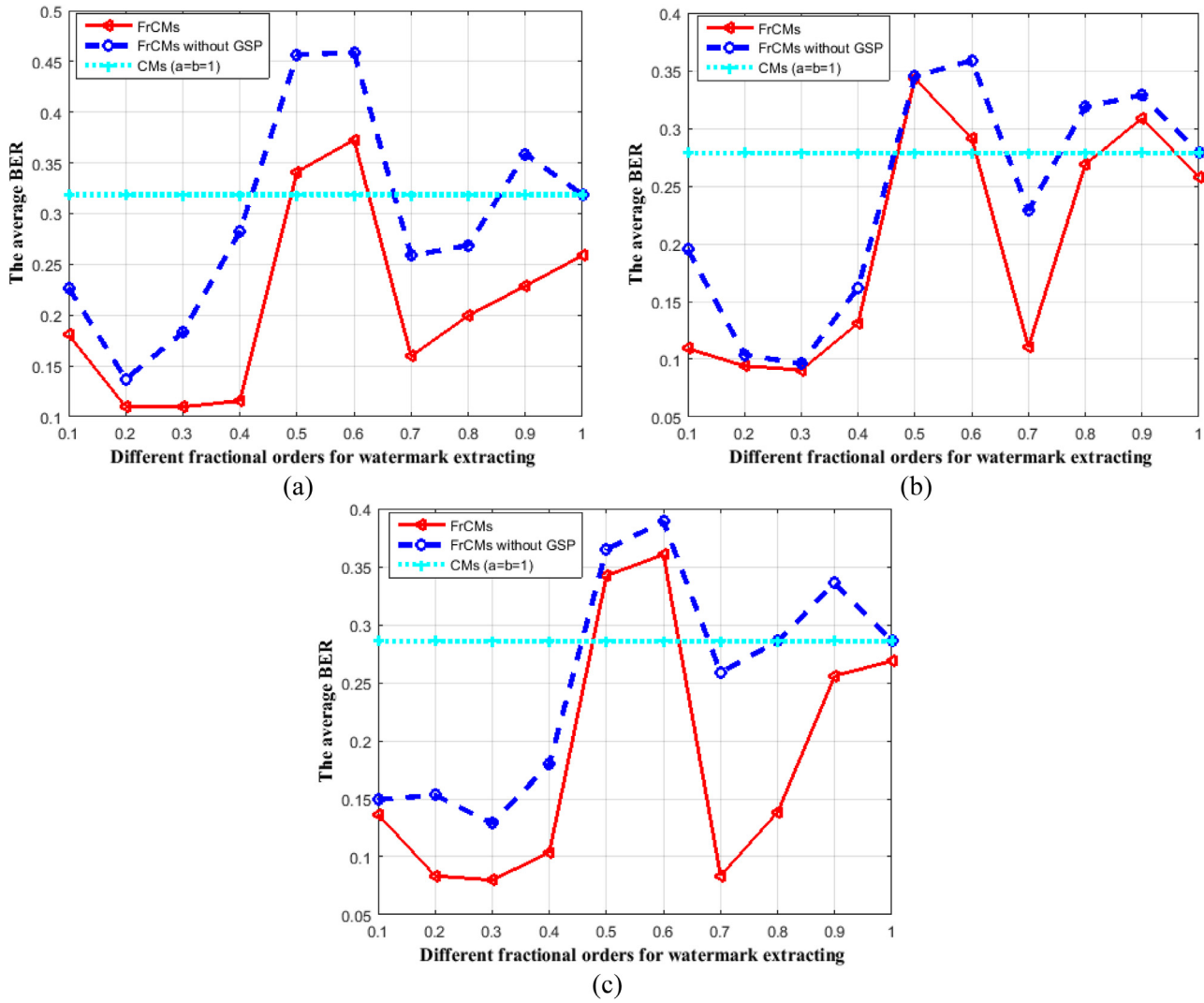
Fig. 12. Average BER of extracted "Horse" watermark with various fractional orders, for combined attacks; (a) Attacks 1, (b) Attacks 2 and (c) Attacks 3.

Fig. 13. Columns 1 to 10 show the extracted "Horse" watermarks with fractional order up to 0.1, 0.2, 0.3, 0.4, 0.5, 0.6, 0.7, 0.8, 0.9, and 1, respectively. In the first row, the fractional orders ($a = b = 0.3$) are used in the watermark insertion phase, and the second row, the fractional orders ($a = b = 0.7$) are used in the watermark insertion phase.

strategy does not use the difference between two adjacent block coefficients to incorporate the watermark bit, and in the case of histogram equalization, the modification of the pixel values of each block has a severe impact on the accuracy of watermarking extraction. Note that, for all attacks, the BERs of the FrCMs-based schema are considerably lower than those of the CMs-based schema, indicating that the proposed schema is robust to different attacks than the one based on the classical CMs.

In terms of comparison between the other schemes, the proposed scheme offers better robustness against most attacks than the schemes based on TMs, KMs, FrKMs, SVD, DFrFT, DFrFT, DFrFT, DFrCT and DFrST, where the BERs of proposed scheme are considerably smaller than those of the other eight watermark schemes.

In the third test, we will show the influence of the variation of the fractional orders on the watermark imperceptibility and the robustness. The "Horse" watermark is embedded in the ten test

images (Fig. 4) in order to generate ten watermarked images. The average PSNR is plotted (Fig. 11) as a function of fractional order ranging from ($a = b = 0.1$) to ($a = b = 1$) with a step of 0.1. The quantization step is $\Delta = 60$, and the average PSNR of FrCMs without GSP and that of classical CMs are also plotted on the same figure for a better comparison.

In addition, the influence of the variation of fractional orders on the watermark robustness is analyzed for the following combined attacks:

Attacks1: Salt & Pepper noise (1%) + Median filtering (3×3)+ JPEG 60.

Attacks2: Salt and Peppers noise (1%) + Average Filtering (3×3) + Scaling (1.2).

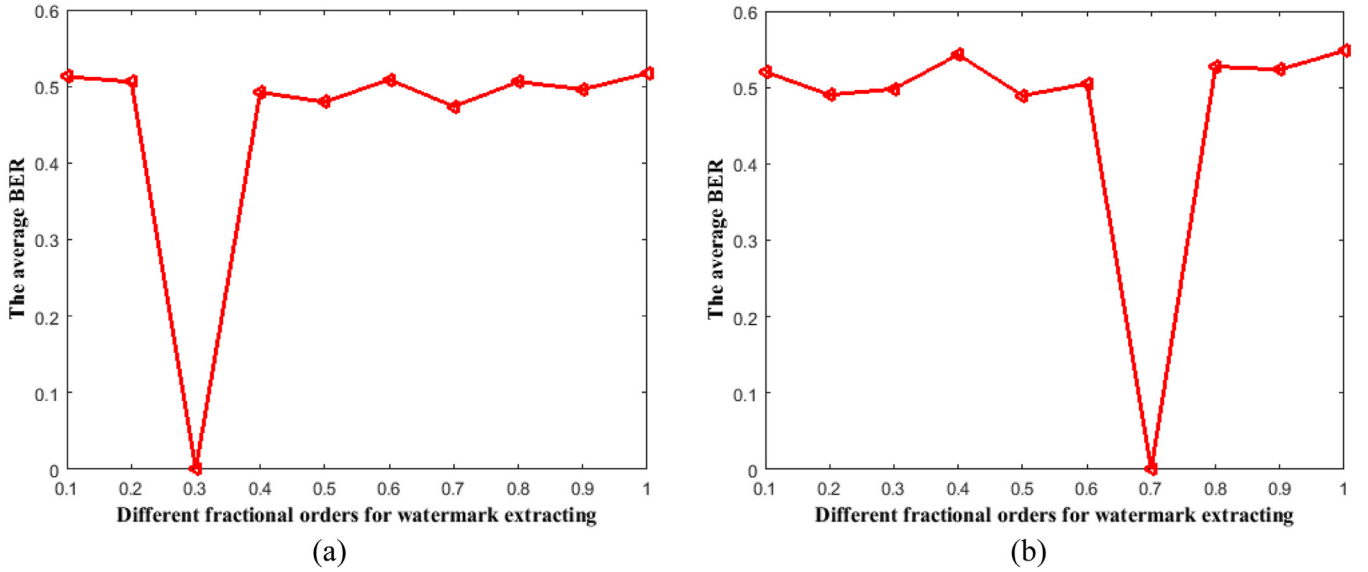Attacks3: Rotation 15° + Gaussian White noise (1%) + Gaussian blur (0.5).

Fig. 14. BER of extracted "Horse" watermark with various fractional orders. (a) Fractional orders ($a = b = 0.3$) are used in the watermark insertion phase, (b) Fractional orders ($a = b = 0.7$) are used in the watermark insertion phase.

The 10 watermarked images are distorted according to these attacks, and the average BER of the extracted "Horse" watermark is plotted against the fractional order in Fig. 12. Note that, the translation and the histogram equalization attacks are not considerate in this test in order to not damage all results.

From the Fig. 11, we can see that our schemes based on FrCMs provide good watermark imperceptibility for most fractional orders than the scheme based on classical CMs, except for some fractional orders ($a = b = 0.5$ and $a = b = 0.6$). In addition, Fig. 12 shows that our schemes are more robust against combined attacks where BERs are very low for most fractional orders than the scheme based on CMs. We can conclude that a better choice of these fractional orders can give the best results in terms of imperceptibility and robustness of the watermark. Note that the GSP greatly improves the results obtained in terms of imperceptibility and robustness of the watermark as shown in Figs 11 and 12.

In the last test, we will show that the proposed FrCMs reinforce the security of the watermark system. The "Male" and "Horse" images are adopted as host and watermark images, respectively, and attacks are not considered in this test. In the watermark insertion phase, the two fractional orders ($a = b = 0.3$) and ($a = b = 0.7$) are used to generate two watermarked images of "Male". In the watermarking extraction phase, the watermark extracted from "Horse" is obtained by using the watermark extraction scheme (Fig. 3) with fractional orders varying from 0.1 to 1 with a step of 0.1. Fig. 13 shows the extracted "Horse" watermarks for different fractional orders, and their corresponding BER values are shown in Fig. 14.

It is clear from these figures that the extracted "Horse" watermark is recognizable only when the same fractional orders (Key1) are used for watermarking insertion and extraction. On the other hand, wrong fractional orders in the watermarking extraction phase give unrecognizable extracted watermarks where their BERs are greater than 0.5.

The results of this subsection justify that the proposed FrCMs constitution a new attractive transformation for watermarking field.

7. Conclusion

In this article, we have proposed a new set of discrete orthogonal moments named fractional Charlier moments FrCMs. The spectral decomposition of the Charlier polynomials is adopted to determine the new fractional Charlier polynomials FrCPs which are used as kernel in FrCMs. The fractional orders of FrCMs give a wide choice in applications where FrCMs are used. The experimental results demonstrated that some better choice of these fractional orders can achieve best results in the fields of reconstruction and watermarking image.

Declaration of Competing Interest

The authors declare no conflict of interest.

Acknowledgement

Appendix A

Proof of property (c). Let λ be an eigenvalue of Charlier polynomial matrix and x the corresponding eigenvector, then $\hat{C}x = \lambda x$, using the *properties (a) and (b)*, we have:

$$x = \hat{C}\hat{C}x = \lambda\hat{C}x = \lambda^2 x \tag{A1}$$

thus

$$(\lambda^2 - 1)x = 0 \tag{A2}$$

The matrix $\hat{C}$ has only two eigenvalues $\{1, -1\}$, The proof of Eq. (19) has been completed

Appendix B

Proof of properties (d–f). Let $\hat{C} \in \mathbb{C}^{N \times N}$ be Charlier polynomial matrix, with their eigenvalues on the diagonal of a diagonal matrix $\Lambda = diag(\lambda_1, \ldots \lambda_N) \in \mathbb{C}^{N \times N}$ and the corresponding eigenvectors forming the columns of a matrix $V = [u_1, \ldots, u_N] \in \mathbb{C}^{N \times N}$, we have:

$$\hat{C} = V \Lambda V^{-1} \tag{B.1}$$

where, the orthonormal vectors $u_1, \ldots u_N$ are eigenvectors of $\hat{C}$, corresponding to eigenvalues $\lambda_1, \ldots \lambda_N$.

$$\hat{C} = [u_1 \cdots u_N] \begin{pmatrix} \lambda_1 & & \\ & \ddots & \\ & & \lambda_N \end{pmatrix} \begin{bmatrix} u_1^T \\ \vdots \\ u_N^T \end{bmatrix} \tag{B.2}$$

$$\hat{C} = [\lambda_1 u_1 \cdots \lambda_N u_N] \begin{bmatrix} u_1^T \\ \vdots \\ u_N^T \end{bmatrix} \tag{B.3}$$

$$\hat{C} = \lambda_1 u_1 u_1^T \cdots \lambda_N u_N u_N^T \tag{B.4}$$

Notice that the matrices

$$P_j := u_j u_j^T \in \mathbb{C}^{N \times N} \tag{B.5}$$

are orthogonal projectors, since $P_j^T = P_j$ and

$$P_j^2 := u_j (u_j^T u_j) u_j^T = u_j u_j^T = P_j$$

$$\hat{C} = \sum_{j=1}^{N} \lambda_j P_j \tag{B.6}$$

if $j \neq k$, then the orthogonality of the eigenvectors implies

$$P_j P_k = u_j u_j^T u_k u_k^T = 0 \tag{B.7}$$

The proof of *properties (d–f)* has been completed.

Proof of propriety (h). Let γ, η and λ be respectively the eigenvalues of the matrices P_1, P_2 and $\hat{C}$ of size $N \times N$, using (29) and (30), we have:

$$\begin{aligned} |\gamma I - P_1| &= |\gamma I - 0.5(\hat{C} + I)| = |(\gamma - 0.5)I - 0.5\hat{C}| \\ &= |(\gamma - 0.5)I - 0.5\hat{C}| = 0.5^N |(2\gamma - 1)I - \hat{C}| \\ &= 0 \end{aligned} \tag{B.8}$$

Similarly, we have

$$|\eta I - P_2| = 0.5^N |(2\eta - 1)I - \hat{C}| = 0 \tag{B.9}$$

and

$$|\lambda I - \hat{C}| = 0 \tag{B.10}$$

From (B.8)–(B.10), we have

$$2\gamma - 1 = \lambda \tag{B.11}$$

$$-(2\eta - 1) = \lambda \tag{B.12}$$

Hence, if $\lambda = 1$, there is $\gamma = 1$, $\eta = 0$, and if $\lambda = -1$, then $\gamma = 0$, $\eta = 1$.

The proof of *propriety (h)* has been completed.

Appendix C

Let P_1 and P_2 the spectral projection matrices of modified Charlier polynomial matrix $\hat{C} \in \mathbb{C}^{N \times N}$, and x, y be their eigenvectors corresponding to $\lambda = 1$, respectively.

Proof of Lemma 1. From Table 1 and *property (g)*, we have:

$$P_1 x = x \tag{C.1}$$

and

$$P_2 y = y \tag{C.2}$$

using (C.1) and (C.2) and *property (f)*, we have:

$$x^T y = (P_1 x)^T (P_2 y) = x^T P_1^T P_2 y = 0 \tag{C.3}$$

The proof of *Lemma 1* has been completed.

Proof of Lemma 2. From Eq. (20), Lemma 1 and property (f) we have:

$$\begin{aligned} \hat{C}x &= (\lambda_1 P_1 + \lambda_2 P_2)x = \lambda_1 P_1 x + \lambda_2 P_2 x \\ &= \lambda_1 P_1 x + \lambda_2 P_2 P_1 x = \lambda_1 P_1 x + \lambda_2 P_2^T P_1 x \\ &= \lambda_1 P_1 x = \lambda_1 x \end{aligned} \tag{C.4}$$

$$\begin{aligned} \hat{C}y &= (\lambda_1 P_1 + \lambda_2 P_2)y = \lambda_1 P_1 y + \lambda_2 P_2 y \\ &= \lambda_1 P_1 P_2 y + \lambda_2 P_2 y = \lambda_2 P_2 y = \lambda_2 y \end{aligned} \tag{C.5}$$

The proof of *Lemma 2* has been completed.

References

[1] H. Zhu, et al., Image representation using separable two-dimensional continuous and discrete orthogonal moments, Pattern Recognit. 45 (4) (2012) 1540–1558.

[2] H. Karmouni, et al., Image reconstruction by Krawtchouk moments via digital filter, in: 2017 Intelligent Systems and Computer Vision (ISCV), 2017, pp. 1–7.

[3] B. Honarvar, et al., Image reconstruction from a complete set of geometric and complex moments, Signal Process. 98 (May) (2014) 224–232, doi:10.1016/j.sigpro.2013.11.037.

[4] H. Rahmalan, et al., Using tchebichef moment for fast and efficient image compression, Pattern Recognit. Image Anal. 20 (4) (2010) 505–512.

[5] G.A. Papakostas, et al., Image coding using a wavelet based Zernike moments compression technique, in: 2002 14th International Conference on Digital Signal Processing Proceedings. DSP 2002 (Cat. No. 02TH8628), 2, 2002, pp. 517–520.

[6] E.D. Tsougenis, et al., Image watermarking via separable moments, Multimed. Tools Appl. 74 (11) (2015) 3985–4012.

[7] X. Liu, et al., Fractional Krawtchouk transform with an application to image watermarking, IEEE Trans. Signal Process. 65 ((7) April) (2017) 1894–1908, doi:10.1109/TSP.2017.2652383.

[8] E.D. Tsougenis, et al., Performance evaluation of moment-based watermarking methods: a review, J. Syst. Softw. 85 (8) (2012) 1864–1884.

[9] E.D. Tsougenis, et al., Introducing the separable moments for image watermarking, in a totaly moment-oriented framework, in: 2013 18th International Conference on Digital Signal Processing (DSP), Fira , Santorini , Greece, 2013, pp. 1–6, doi:10.1109/ICDSP.2013.6622813.

[10] L. Zhang, et al., Geometric invariant blind image watermarking by invariant tchebichef moments, Opt. Express 15 (5) (2007) 2251, doi:10.1364/OE.15.002251.

[11] L.-M. Luo, et al., A modified moment-based edge operator for rectangular pixel image, IEEE Trans. Circuits Syst. Video Technol. 4 (6) (1994) 552–554.

[12] M. Alghoniemy, et al., Geometric distortion correction through image normalization, in: 2000 IEEE International Conference on Multimedia and Expo. ICME2000. Proceedings. Latest Advances in the Fast Changing World of Multimedia (Cat. No. 00TH8532), 3, 2000, pp. 1291–1294.

[13] A. Hmimid, et al., Fast computation of separable two-dimensional discrete invariant moments for image classification, Pattern Recognit. 48 (2) (2015) 509–521.

[14] A.F. Nikiforov, et al., Classical orthogonal polynomials of a discrete variable, in: Classical Orthogonal Polynomials of a Discrete Variable, Springer, 1991, pp. 18–54.

[15] C.-W. Chong, et al., Translation and scale invariants of Legendre moments, Pattern Recognit. 37 ((1) January) (2004) 119–129, doi:10.1016/j.patcog.2003.06.003.

[16] A. Khotanzad, et al., Invariant image recognition by Zernike moments, IEEE Trans. Pattern Anal. Mach. Intell. 12 ((5) May) (1990) 489–497, doi:10.1109/34.55109.

[17] K.M. Hosny, Image representation using accurate orthogonal Gegenbauer moments, Pattern Recognit. Lett. 32 ((6) April) (2011) 795–804, doi:10.1016/j.patrec.2011.01.006.

[18] Y. Sheng, et al., Orthogonal Fourier–Mellin moments for invariant pattern recognition, JOSA A 11 ((6) June) (1994) 1748–1757, doi:10.1364/JOSAA.11.001748.

[19] B.H.S. Asli, et al., New discrete orthogonal moments for signal analysis, Signal Process 141 (2017) 57–73.

[20] R. Mukundan, et al., Image analysis by Tchebichef moments, IEEE Trans. Image Process. 10 (9) (2001) 1357–1364.

[21] B. Honarvar, et al., Fast computation of Krawtchouk moments, Inf. Sci. 288 (December) (2014) 73–86, doi:10.1016/j.ins.2014.07.046.

[22] H. Karmouni, et al., Image analysis using separable Krawtchouk–Tchebichef's moments, in: 2017 International Conference on Advanced Technologies for Signal and Image Processing (ATSIP), 2017, pp. 1–5.

[23] A. Mesbah, et al., Fast algorithm for 3D local feature extraction using Hahn and Charlier moments, in: International Symposium on Ubiquitous Networking, 2016, pp. 357–373.

[24] H. Zhu, et al., General form for obtaining discrete orthogonal moments, IET Image Process 4 (5) (2010) 335, doi:10.1049/iet-ipr.2009.0195.

[25] H. Karmouni, et al., Fast and stable computation of the Charlier moments and their inverses using digital filters and image block representation, Circuits Syst. Signal Process. 37 ((9) September) (2018) 4015–4033, doi:10.1007/s00034-018-0755-2.

[26] P. Yap, et al., IEEE Trans. Pattern Anal. Mach. Intell. 29 ((11) November) (2007) 2057–2062, doi:10.1109/TPAMI.2007.70709.

[27] M. Sayyouri, et al., A fast computation of novel set of meixner invariant moments for image analysis, Circuits Syst. Signal Process. 34 ((3) March) (2015) 875–900, doi:10.1007/s00034-014-9881-7.

[28] H.M. Ozaktas, et al., The fractional fourier transform, in: 2001 European Control Conference (ECC), 2001, pp. 1477–1483, doi:10.23919/ECC.2001.7076127.

[29] S.-C. Pei, et al., Closed-form discrete fractional and affine Fourier transforms, IEEE Trans Signal Process. 48 (2000) 1338–1353, doi:10.1109/78.839981.

[30] S.-C. Pei, et al., The discrete fractional cosine and sine transforms, IEEE Trans. Signal Process. 49 (6) (2001) 1198–1207.

[31] B. Xiao, et al., Image analysis by fractional-order orthogonal moments, Inf. Sci. 382–383 (March) (2017) 135–149, doi:10.1016/j.ins.2016.12.011.

[32] H. Zhang, et al., Fractional orthogonal Fourier–Mellin moments for pattern recognition, in: Chinese Conference on Pattern Recognition, 2016, pp. 766–778.

[33] K. Parand, et al., Novel orthogonal functions for solving differential equations of arbitrary order, Tbilisi Math. J. 10 ((1) January) (2017) 31–55, doi:10.1515/tmj-2017-0004.

[34] R. Benouini, et al., Fractional-order orthogonal Chebyshev moments and moment invariants for image representation and pattern recognition, Pattern Recognit 86 (February) (2019) 332–343, doi:10.1016/j.patcog.2018.10.001.

[35] P.-T. Yap, et al., Image analysis by Krawtchouk moments, IEEE Trans. Image Process. 12 (11) (2003) 1367–1377.

[36] M. Sayyouri, et al., Image analysis using separable discrete moments of Charlier–Hahn, Multimed. Tools Appl. 75 ((1) January) (2016) 547–571, doi:10.1007/s11042-014-2307-5.

[37] H. Amakdouf, et al., Classification and recognition of 3D image of Charlier moments using a multilayer perceptron architecture, Procedia Comput. Sci. 127 (January) (2018) 226–235, doi:10.1016/j.procs.2018.01.118.

[38] T. Jahid, et al., Fast algorithm of 3D discrete image orthogonal moments computation based on 3D cuboid, J. Math. Imaging Vis. 61 (4) (2019) 534–554.

[39] H. Karmouni, et al., Fast reconstruction of 3D images using charlier discrete orthogonal moments, Circuits Syst. Signal Process. 38 ((8) August) (2019) 3715–3742, doi:10.1007/s00034-019-01025-0.

[40] T.S. Chihara, An Introduction to Orthogonal Polynomials, Courier Corporation, 2011.

[41] H. Zhu, et al., Image descriptions with nonseparable two-dimensional Charlier and Meixner moments, Int. J. Pattern Recognit. Artif. Intell. 25 ((01) February) (2011) 37–55, doi:10.1142/S0218001411008506.

[42] C. Camacho-Bello, et al., Some computational aspects of Tchebichef moments for higher orders, Pattern Recognit. Lett. 112 (September) (2018) 332–339, doi:10.1016/j.patrec.2018.08.020.

[43] D.S. Watkins, The Matrix Eigenvalue Problem: GR and Krylov Subspace Methods, Society for Industrial and Applied Mathematics, Philadelphia, 2007.

[44] S.H. Friedberg, et al., Linear Algebra, Pearson, Essex, 2014.

[45] G.W. Stewart, Introduction to Matrix Computations, Elsevier, 1973.

[46] S.-C. Pei, et al., Discrete fractional fourier transform based on orthogonal projections, IEEE Trans. Signal Process. 47 (5) (1999) 1335–1348.

[47] A.M. Al-Haj, Advanced Techniques in Multimedia watermarking: image, Video and Audio applications: image, Video and Audio Applications, IGI Global, 2010.

[48] A. Poljicak, et al., Discrete Fourier transform-based watermarking method with an optimal implementation radius, J. Electron. Imaging 20 (3) (2011) 033008.

[49] J.R. Hernandez, et al., DCT-domain watermarking techniques for still images: detector performance analysis and a new structure, IEEE Trans. Image Process. 9 (1) (2000) 55–68.

[50] J.-M. Guo, et al., False-positive-free SVD-based image watermarking, J. Vis. Commun. Image Represent. 25 ((5) July) (2014) 1149–1163, doi:10.1016/j.jvcir.2014.03.012.

[51] B. Chen, et al., Full 4-D quaternion discrete Fourier transform based watermarking for color images, Digit. Signal Process. 28 (2014) 106–119.

[52] C. Deng, et al., A local Tchebichef moments-based robust image watermarking, Signal Process 89 ((8) August) (2009) 1531–1539, doi:10.1016/j.sigpro.2009.02.005.

[53] B.L. Gunjal, et al., An overview of transform domain robust digital image watermarking algorithms, J. Emerg. Trends Comput. Inf. Sciences 2 (1) (2010) 37–42.

[54] L. Wu, et al., Arnold transformation algorithm and anti-arnold transformation algorithm, in: 2009 First International Conference on Information Science and Engineering, Nanjing, China, 2009, pp. 1164–1167, doi:10.1109/ICISE.2009.347.

[55] L.I. Xu-dong, Optimization analysis of formulas for quantization-based image watermarking [J], Opto-Electron. Eng. 37 (2) (2010) 96–102.

[56] H.-Y. Yang, et al., Robust color image watermarking using geometric invariant quaternion polar harmonic transform, ACM Trans. Multimed. Comput. Commun. Appl. 11 ((3) February) (2015) pp. 40:1–40:26, doi:10.1145/2700299.

[57] Z. Li, et al., Geometric distortions invariant blind second generation watermarking technique based on Tchebichef moment of original image, J. Softw. 18 (9) (2007) 2283–2294.

[58] "Shape matching/retrieval." [Online]. Available: http://www.dabi.temple.edu/~shape/MPEG7/dataset.html. [Accessed: 14-Jul-2019].

[59] M. Yamni, et al., Influence of Krawtchouk and Charlier moment's parameters on image reconstruction and classification, Procedia Comput. Sci. 148 (2019) 418–427.

[60] O. El ogri, et al., 2D and 3D Medical Image Analysis by Discrete Orthogonal Moments, Procedia Comput. Sci. 148 (2019) 428–437.

[61] M. Sayyouri, et al., Image classification using separable invariant moments of Krawtchouk-Tchebichef, Int. Conf. Comput. Syst. Appl. (2015) 1–6.

[62] T. Jahid, et al., Image moments and reconstruction by Krawtchouk via Clenshaw's reccurence formula, Int. Conf. Electrical Inf. Technol. (2017) 1–7.

[63] M. Sayyouri, et al., Improving the performance of image classification by Hahn moment invariants, JOSA A (2013) 2381–2394.

[64] H. Karmouni, et al., Fast computation of inverse Meixner moments transform using Clenshaw's formula, Multimed. Tools Appl. (2019) 31245–31265.

[65] H. Karmouni, et al., Fast Reconstruction of 3D Images Using Charlier Discrete Orthogonal Moments., Circuits Syst. Signal Process. (2019) 3715–3742.

[66] M. Sayyouri, et al., A fast computation of Hahn moments for binary and gray-scale images, Int. Conf. Complex Syst. (2012) 1–6.